Nanoscale

RSC Publishing

PAPER

View Article Online
View Journal | View Issue

Cite this: *Nanoscale*, 2013, **5**, 6960

Free-standing and binder-free lithium-ion electrodes based on robust layered assembly of graphene and Co_3O_4 nanosheets†

Ronghua Wang, Chaohe Xu, Jing Sun,* Yangqiao Liu, Lian Gao and Chucheng Lin

Received 21st March 2013
Accepted 19th May 2013

DOI: 10.1039/c3nr01392h

www.rsc.org/nanoscale

Free-standing and binder-free Co_3O_4/graphene films were fabricated through vacuum filtration and thermal treatment processes, in which sheet-like Co_3O_4 and graphene were assembled into a robust lamellar hierarchical structure *via* electrostatic interactions. The morphological compatibility coupled with strong interfacial interactions between Co_3O_4 and graphene significantly promoted the interfacial electron and lithium ion transport. When used as a binder-less and free-standing electrode for lithium-ion batteries, the hybrid film delivered a high specific capacity (~1400 mA h g^{-1} at 100 mA g^{-1} based on the total electrode weight), enhanced rate capability and excellent cyclic stability (~1200 mA h g^{-1} at 200 mA g^{-1} after 100 cycles). This effective strategy will provide new insight into the design and synthesis of many other composite electrodes for high-performance lithium-ion batteries.

1 Introduction

Rechargeable lithium-ion batteries (LIBs), owing to their high energy density, long cyclic life and environmental benignity, have been envisioned as the most attractive energy storage system for applications in portable electronics, electric vehicles and so on.[1–5] In order to satisfy the increasing demand for higher energy density LIBs, novel electrode materials and architectures are intensively investigated.[6–9] Among the available anode materials, Co_3O_4 attracts extensive interest due to its high theoretical capacity (890 mA h g^{-1}), which is more than two times larger than that of graphite (372 mA h g^{-1}).[10–12] However, its large volume expansion/contraction and severe particle aggregation associated with the Li^+ insertion and extraction process lead to electrode pulverization, electric contact loss with the current collector and, consequently, result in a large reversible capacity loss and poor cycling stability.[13–16] Generally, there are two strategies to solve these problems. One focuses on fabricating various nanostructures, such as nanotubes,[17] nanowires,[18,19] nanorods,[20,21] octahedral cages,[10,22] hollow spheres,[23] nanoneedles[24] and nanosheets,[15,25–27] to mitigate the pulverization. Another approach is to construct composites with carbon materials to further enhance the structure stability and electrical conductivity.[28–30]

Graphene sheets (GS), with high conductivity, large specific surface area and superior mechanical properties, can provide a support for anchoring nanocrystals and work as a highly conductive matrix.[31–34] Recently, composites of Co_3O_4 with graphene were successfully prepared as anode materials for LIBs and greatly improved the lithium storage properties.[16,35–38] For example, Cheng and coworkers[39] reported a hydrothermal method to synthesize the composite of graphene anchored with Co_3O_4 nanoparticles, which exhibited a capacity of 800 mA h g^{-1} at 50 mA g^{-1}. Yang *et al.*[40] adopted a two-step process involving nanocasting and a self-assembly approach to prepare graphene encapsulated mesoporous Co_3O_4 microspheres. The composite delivered a capacity of 820 mA h g^{-1} at 100 mA g^{-1}. In these previous studies, electrodes were usually prepared with active materials, carbon black and a polymer binder for the battery test. Evidently, a polymer binder may block the diffusion channels of ion transportation and the outstanding electric performance of graphene had been significantly impaired.[14,28,41,42]

Until now, great efforts have been devoted to prepare graphene-based free-standing and binder-free electrodes. For instance, a flexible graphene film was used as a current collector, upon which metal oxides were attached by chemical deposition[41,43] or hydrothermal reaction.[44] Such approaches usually produce low loading and aggregation of metal oxides, thus the improvement in the overall hybrid electrode performance is limited. Another way is based on vacuum filtration, by which various active materials (such as TiO_2,[45] MnO_2,[42,46] V_2O_5 (ref. 47) and silicon[48–50]) were incorporated into a graphene scaffold.[42,51] Specifically, both components were homogeneously mixed and filtered to produce paper-like electrodes.

The State Key Lab of High Performance Ceramics and Superfine Microstructure, Shanghai Institute of Ceramics, Chinese Academy of Sciences, 1295 Dingxi Road, Shanghai 200050, P.R. China. E-mail: jingsun@mail.sic.ac.cn; Fax: +86-21-52413122; Tel: +86-21-52414301

† Electronic supplementary information (ESI) available: See DOI: 10.1039/c3nr01392h

Graphene formed a three-dimensional conductive network to behave as a mechanical support and an embedded-in current collector. At present, active nanomaterials are limited to 0D nanocrystals,[48,52,53] 1D nanotubes[46] and nanowires.[47,49,50] On one hand, these active materials are made in point-to-point or line-to-line contact with graphene, and the electrical contact area between them is rather limited. On the other hand, they are just physically contacted with graphene without any strong interfacial interactions. These two aspects resulted in an inferior electron transport through graphene to active materials. In this regard, it is highly desirable to engineer the interfacial interactions between the support and active materials.

Herein, we firstly propose a strategy to strengthen interfacial interactions by assembling GS with 2D Co_3O_4 nanosheets into a lamellar hierarchical structure with the aid of electrostatic attractive interactions. The unique feature of the sheet-to-sheet assembly (2D–2D) is that each Co_3O_4 nanosheet will have maximum electrical contact with graphene, which could result in high conductivity of the hybrids. Moreover, strong interfacial interactions between Co_3O_4 and graphene contribute to a robust linking between the two components, which further promoted interfacial electron and lithium ion transport. Benefitting from the morphological compatibility and intimate integration between Co_3O_4 and graphene, the binder-free and free-standing hybrid electrode exhibited significantly enhanced lithium storage properties in terms of higher specific capacities, better cyclic stability and rate capability compared to traditional binder-containing electrodes and pure Co_3O_4 electrodes. To the best of our knowledge, this is the first demonstration of a self-supporting binder-free anode prototype with a lamellar hierarchical structure and strong interfacial interaction, which is totally different from previously reported graphene-based hybrid films.[42,45–50]

2 Experimental

2.1 Material preparation

(a) Preparation of β-Co(OH)$_2$. Synthesis of β-$Co(OH)_2$ was performed according to previous literature.[54] In a typical procedure, $CoCl_2 \cdot 6H_2O$ (238 mg) and hexamethylenetetramine (HMT) (1.68 g) were dissolved in a mixed solution containing 180 mL de-ionized water and 20 mL ethanol. The solution was then heated at 90 °C for 1 h under magnetic stirring. The product was filtered, washed with de-ionized water and anhydrous ethanol several times, and finally air-dried at room temperature.

(b) Preparation of Co_3O_4/GS hybrid films and pure Co_3O_4. Graphene oxide (GO) was synthesized from graphite by a modified Hummers method.[55] The as-prepared $Co(OH)_2$ can readily be dispersed in water to form a pink colored homogeneous dispersion. By mixing $Co(OH)_2$ dispersion with GO aqueous dispersion under sonication, a flocculent solution was obtained, which was vacuum-filtered using anodisc membrane filters (47 mm in diameter, 0.2 μm). Afterwards, a free-standing $Co(OH)_2$/GO hybrid film can be obtained after drying and peeling off from the filter membrane. Finally, the as-prepared $Co(OH)_2$/GO hybrid films were annealed at 350 °C in argon for 2 h to obtain CoO/GS, which were further converted to Co_3O_4/GS *via* annealing at 300 °C in air for 2 h. In this work, the $Co(OH)_2$/GO mass ratio was varied as 1 : 2, 1 : 1 and 2 : 1 to optimize the lithium storage performance. Detailed discussions were carried out on the optimized sample $Co(OH)_2$/GO (1 : 1) with 75% Co_3O_4.

A control sample of bare Co_3O_4 was prepared by the heat treatment of pure $Co(OH)_2$ at 350 °C in argon for 2 h and 300 °C in air for another 2 h afterwards.

2.2 Electrode preparation

Co_3O_4/GS hybrid films were directly used as a free-standing electrode without any binder or additive (named F-Co_3O_4/GS). The mass loading was ~1.6 mg cm^{-2} for F-Co_3O_4/GS. A Co_3O_4/GS traditional electrode, named T-Co_3O_4/GS, was prepared by conventional slurry-coating technology. Specifically, Co_3O_4/GS hybrid films were first ground into powders, which were mixed with carbon black and poly(vinyldifluoride) (PVDF) at a weight ratio of 80 : 10 : 10 in *N*-methylpyrrolidone (NMP) to form slurries. The homogeneous slurries were then pasted on a copper current collector and dried under vacuum at 110 °C for 12 h. Another control electrode, named T-Co_3O_4, was prepared by the same slurry-coating technology. The mass loading was ~1.2 mg cm^{-2} for T-Co_3O_4/GS and T-Co_3O_4.

2.3 Material characterization

The morphology was characterized with a transmission electron microscope (JEM-2100F, JEOL, Tokyo, Japan). The field-emission scanning electron microscopy (FE-SEM) analysis was performed on a JSM-6700F at an acceleration voltage of 10.0 kV. X-ray diffraction (XRD) was carried out on a D/max 2550V X-ray diffraction-meter with Cu-Kα irradiation at λ = 1.5406. Thermogravimetric analysis (TGA) was conducted in air at a heating rate of 10 °C min^{-1}. Fourier transform infrared spectroscopy (FTIR) and Raman spectroscopy were recorded on a Nicolet 7000-C and DXR Raman Microscope, Thermal Scientific Corporation, USA, with a 532 nm excitation length respectively. X-ray photoelectron spectroscopy (XPS) analysis was conducted using a twin anode gun, Mg Kα (1253.6 eV) (Microlab 310F Scanning Auger Microprobe, VG SCIENTIFIC LTD). The conductivity of the Co_3O_4/GS hybrid film was measured by a four-point probe method in the van der Pauw configuration with an Accent HL5500 system. The surface electrokinetic properties of $Co(OH)_2$ and GO were characterized by zeta potential measurements. N_2 adsorption/desorption isotherms were determined using a Micromeritics ASAP2010 Analyzer (USA).

2.4 Electrochemical measurements

Cyclic voltammetry (CV) was carried out in the voltage range of 0–3.0 V with a scan rate of 0.5 mV s^{-1}. The electrochemical impedance spectroscopy (EIS) measurements were carried out on the samples with a PARSTAT 2273, using a sine wave of 10 mV over a frequency range of 100 KHz–0.01 Hz. The electrochemical properties of the electrodes (F-Co_3O_4/GS, T-Co_3O_4/GS and T-Co_3O_4) were characterized at room temperature. Li foil

was used as the counter electrode. The electrolyte was 1 M $LiPF_6$ in a 50 : 50 w/w mixture of ethylene carbonate (EC) and dimethyl carbonate (DMC). Cell assembly was carried out in a glove box with the concentrations of moisture and oxygen below 1 ppm. The batteries were measured using a CT2001 battery tester.

3 Results and discussion

The fabrication process for Co_3O_4/GS hybrid films is depicted in Fig. 1a. When GO dispersion was added, the pink colored $Co(OH)_2$ dispersion turned into a flocculent solution, and a brown precipitate was formed at the bottom after keeping it still for ~30 min (Fig. 1b). GO could be considered as a negatively charged sheet due to the presence of carboxyl groups (zeta potential: −45 mV), while $Co(OH)_2$ is positively charged with a zeta potential of 21.7 mV. This indicates that the electrostatic attractive interaction is the driving force for the self-assembly of the two dispersions.[40,56–61] A free-standing hybrid film with a diameter of *ca.* 42 mm can be obtained by filtration of the precipitate and heat treatment (Fig. 1c). Importantly, the sheet-to-sheet assembly (2D–2D) could endow the precipitate with an excellent film-forming ability. In this study, when the $Co(OH)_2$/GO mass ratio ranged from 1 : 2 to 4 : 1, the composites could easily form free-standing films. This feature is much superior to those of 0D–2D and 1D–2D assembly, and favorable to optimize the properties of the composite.

The crystallographic structure and phase purity were analyzed by XRD. As shown in Fig. 2, XRD patterns of $Co(OH)_2$ can be well indexed as brucite-like β-$Co(OH)_2$ (Fig. 2a, JCPDS no. 74-1057). With heat treatment in an inert atmosphere, the $Co(OH)_2$/GO phase transformed into CoO/GS (Fig. 2b, JCPDS no. 74-2392). After annealing in air, all the diffraction peaks can be assigned to the face-centered cubic Co_3O_4 (Fig. 2c, JCPDS no. 42-1467), indicating that CoO has turned completely into Co_3O_4.

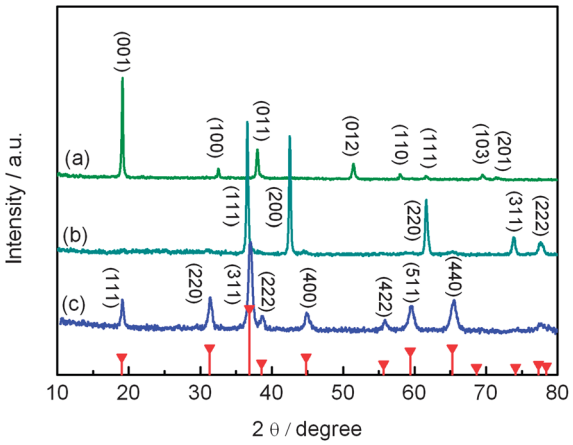

Fig. 2 XRD curves of the as synthesized $Co(OH)_2$/GO (a), CoO/GS (b) and Co_3O_4/GS films (c).

The changes in chemical composition of $Co(OH)_2$/GO during heat treatment are further characterized by XPS. The Co 2p spectrum of $Co(OH)_2$/GO showed two major peaks at 781.6 and 796.9 eV, assigned to the Co $2p_{3/2}$ and Co $2p_{1/2}$,[62] respectively (Fig. 3a). For CoO/GS, the Co $2p_{3/2}$ and Co $2p_{1/2}$ peaks shifted to 780.7 and 796.6 eV, accompanied by two prominent shake-up satellite peaks (786.1 and 802.7 eV). These are the typical characteristic peaks of CoO,[29] demonstrating the transformation of $Co(OH)_2$ to CoO, while the Co_3O_4/GS hybrid film exhibited two peaks at 780.2 and 795.6 eV with a spin–orbit splitting of 15.4 eV, distinctly verifying the formation of Co_3O_4.[21,39] The formation of Co_3O_4 can be further confirmed by the O 1s peak at 529.9 eV (see ESI, Fig. S1†), which corresponds to the oxygen species in Co_3O_4.[21,39,44]

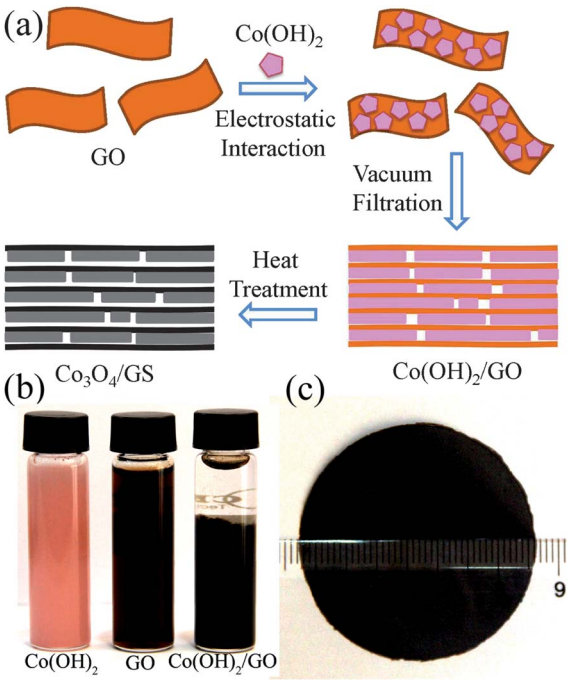

Fig. 1 (a) The fabrication process for Co_3O_4/GS hybrid films; (b) digital photographs of $Co(OH)_2$ dispersion, GO dispersion and $Co(OH)_2$/GO suspension; (c) digital photographs of a free-standing Co_3O_4/GS hybrid film.

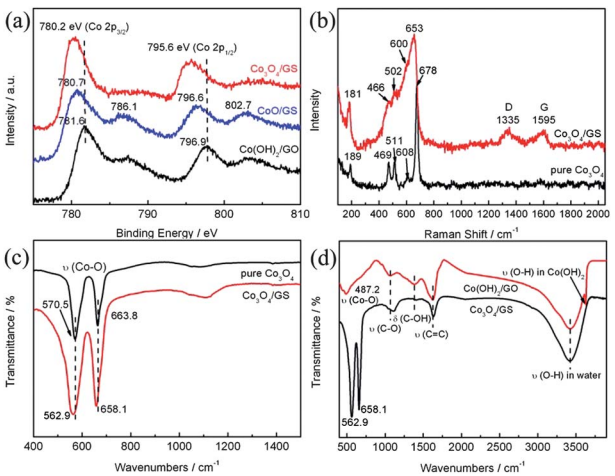

Fig. 3 (a) Co 2p XPS spectra; (b and c) Raman spectra and FTIR spectra of pure Co_3O_4 and Co_3O_4/GS hybrid film; (d) FTIR spectra of $Co(OH)_2$/GO and Co_3O_4/GS.

Raman spectra and FTIR were employed to investigate the interfacial interactions between Co_3O_4 and graphene. As shown in Fig. 3b, the Raman spectrum of pure Co_3O_4 exhibited four characteristic peaks at 469, 511, 608, and 678 cm^{-1}, corresponding to E_g, F^1_{2g}, F^2_{2g}, and A^1_g modes of the crystalline Co_3O_4,[11] respectively. As for the Co_3O_4/GS hybrid film, the characteristic peaks of Co_3O_4 showed red shifts compared with those of pure Co_3O_4, revealing the n-type doping effect on Co_3O_4.[53] This indicates significant electronic interactions between Co_3O_4 and graphene. Moreover, in the FTIR spectrum of Co_3O_4/GS (Fig. 3c), the specific peaks representing Co_3O_4 adsorption bands (562.9 and 658.1 cm^{-1}) also underwent a red shift compared with that of pure Co_3O_4 (570.5 and 663.8 cm^{-1}).[36,63] This further confirmed a strong interfacial interaction existing between Co_3O_4 and graphene. Accordingly, the strong interfacial interaction will have a great impact on the interfacial electron and lithium ion transport.

FTIR was further used to analyze the reduction of GO (Fig. 3d). The peaks centered at 1623, 1385 and 1069 cm^{-1} were attributed to C=C, C–OH and C–O functionalities in GO,[13] respectively. Obviously, the intensity of peaks for oxygen-containing functional groups strongly declined for Co_3O_4/GS, indicating the effective reduction of graphene. As a result, the electrical conductivity of the hybrid film reached 794.9 S m^{-1}. It means graphene can serve as an efficient electrically conducting network. Thus, from the above analyses, it is reasonable to conclude that the Co_3O_4/GS hybrid film, with both high conductivity and strong interfacial interactions, was successfully prepared.

The morphology of $Co(OH)_2$ and the mixed suspension was investigated by SEM and TEM (Fig. 4). $Co(OH)_2$ displayed a sheet-like structure with a thickness of ~18 nm (Fig. 4a and b). As shown in Fig. 4c–e. $Co(OH)_2$ nanosheets were uniformly distributed on the surface of GO. It is noteworthy that even after a long time of sonication during the preparation of the TEM specimen, $Co(OH)_2$ nanosheets were still tightly anchored on the surface of GO, suggesting a strong interaction between $Co(OH)_2$ and GO. The HRTEM image displayed that $Co(OH)_2$ was highly crystallized with a lattice spacing of *ca.* 2.75 Å assigned to the interspacing of the (100) crystal planes (Fig. 4f). The corresponding SAED patterns showed perfect hexagonally arranged diffraction spots, which represented the single crystalline nature of $Co(OH)_2$.

Fig. 5 exhibits the cross-sectional SEM images of the hybrid films. It is clear that $Co(OH)_2$ nanosheets and GO tightly aligned in parallel to form an ordered layer structure. Both of them are distributed homogeneously in the hybrid film (Fig. 5a and b). The morphology of CoO/GS is quite similar to that of $Co(OH)_2$/GO (Fig. 5c and d). However, the Co_3O_4/GS film became a loosely stacked layered structure with some open voids formed. The thickness of Co_3O_4 was about 20 nm, which is helpful to shorten the lithium ion diffusion length.[64] In contrast, in the case of pure Co_3O_4, the size increased significantly (Fig. S2,† thickness of about 100 nm) due to the Ostward ripening[47] during the same annealing process. This drastic morphological difference highlights the important role of graphene in restricting the growth of Co_3O_4 during heat treatment. It is noteworthy that

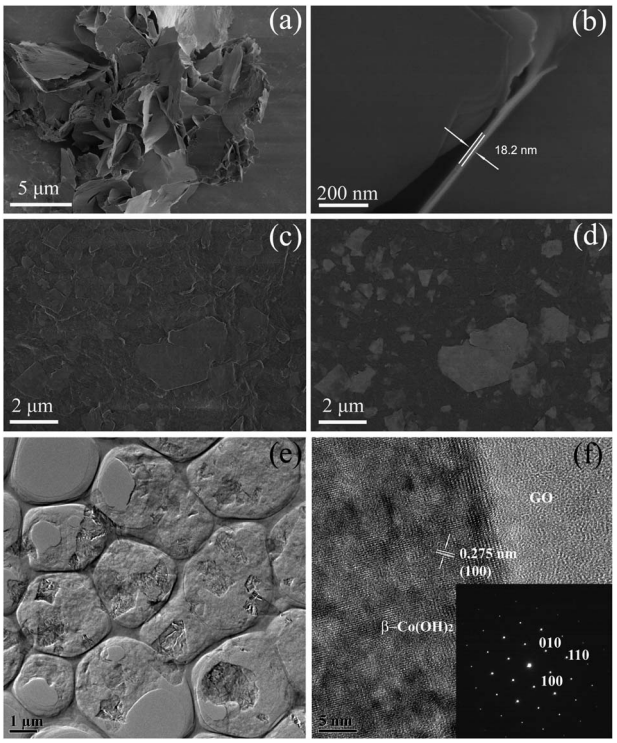

Fig. 4 (a and b) SEM images of $Co(OH)_2$; (c and d) SEM image and the corresponding backscattered SEM image of $Co(OH)_2$/GO suspension showing that $Co(OH)_2$ was well dispersed within GO; (e and f) TEM and HRTEM images of $Co(OH)_2$/GO suspension, the inset in (f) is the SAED pattern of $Co(OH)_2$.

Co_3O_4 and graphene remained tightly contacted with each other. The intimate integration enables fast electron transport through GS to Co_3O_4 sheets. Additionally, such a sheet-to-sheet assembly (2D–2D) can give rise to a maximum interfacial

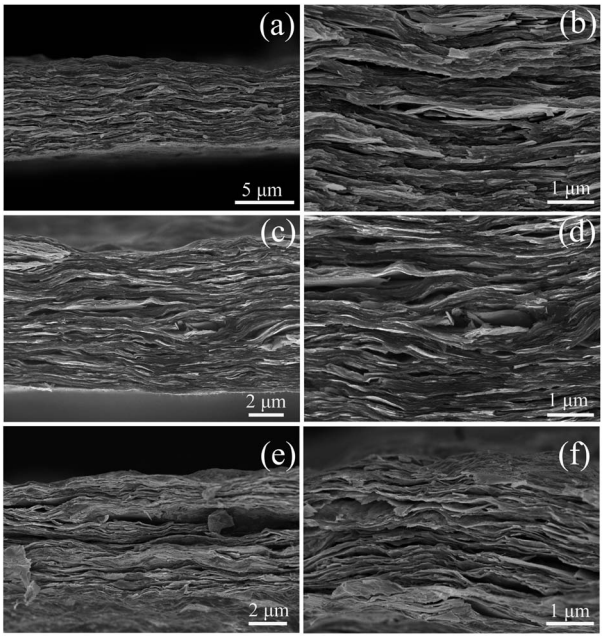

Fig. 5 Cross-sectional SEM images of the $Co(OH)_2$/GO film (a and b), CoO/GS film (c and d) and Co_3O_4/GS film (e and f).

contact between Co_3O_4 and GS compared with 0D–2D and 1D–2D connections. This can further improve electron transport within the hybrid film during lithiation and delithiation processes.

Further insight into the morphology and microstructure of the hybrid was obtained from TEM images. Co_3O_4 nanosheets were still anchored on the surface of graphene (Fig. 6a and b), which is consistent with the SEM images. Closer observation showed that the nanosheets were porous with a pore size of about several nanometers (Fig. 6c). This will greatly increase the specific surface area and lead to a great enhancement in electrochemical activities. HRTEM showed a well-defined crystalline structure with a lattice spacing of 0.467 nm, corresponding to the (111) plane of Co_3O_4 (Fig. 6d). The SAED pattern revealed a single crystal structure of the Co_3O_4 sheet.

The porous structure of the hybrid film was also verified by BET measurement. The Co_3O_4/GS film exhibited type IV nitrogen adsorption and desorption isotherms (Fig. 7a), indicating the presence of mesopores. The specific surface area was 86.6 $m^2\ g^{-1}$, higher than those of CoO/GS (Fig. 7b, 73.9 $m^2\ g^{-1}$) and pure Co_3O_4 (Fig. 7c, 48.7 $m^2\ g^{-1}$). Such a structure can provide not only fast electronic and ionic conducting channels but also sufficient buffer space for the volume expansion of Co_3O_4.[65] Therefore, the Co_3O_4/GS hybrid film provides critical features for high performance electrodes: short diffusion length for Li^+, fast electron and Li^+ transport, large surface reaction sites and excellent endurance for internal stress. The optimal content of Co_3O_4 in the hybrid film was about 75% as determined by TG analysis (Fig. S3† and 7d).

Coin cells were fabricated to measure the electrochemical performance of Co_3O_4/GS hybrid films. Detailed discussions were carried out on the optimized sample with a Co_3O_4 content of 75% hereafter. Here, a graphene conductive network can act as a highly conductive pathway for electrons/lithium ions and as a current collector, without the use of an insulating binder or a conducting additive. Charge storage behaviour was first characterized by CV (Fig. 8a). In the first cycle, one cathodic peak at 0.66 V can be attributed to the electrochemical reduction reaction of Co_3O_4 and the formation of a solid electrolyte interphase (SEI).[20,30] The anodic peak at 2.22 V corresponded to the reversible oxidation of Co^0 to Co_3O_4.[66,67] The reversible reaction occurring with lithium can be described by the following electrochemical conversion reactions:

$$Co_3O_4 + 8Li^+ + 8e^- \rightarrow 3Co + 4Li_2O \quad (1)$$

$$Co + Li_2O \rightarrow CoO + 2Li^+ + 2e^- \quad (2)$$

In the subsequent cycles, the main reduction peak shifted to ~0.85 V while the main anodic peak at ~2.2 V showed very little modification. The peak intensity and integral areas were nearly identical, suggesting the good reversibility of lithium insertion and extraction reactions.[21]

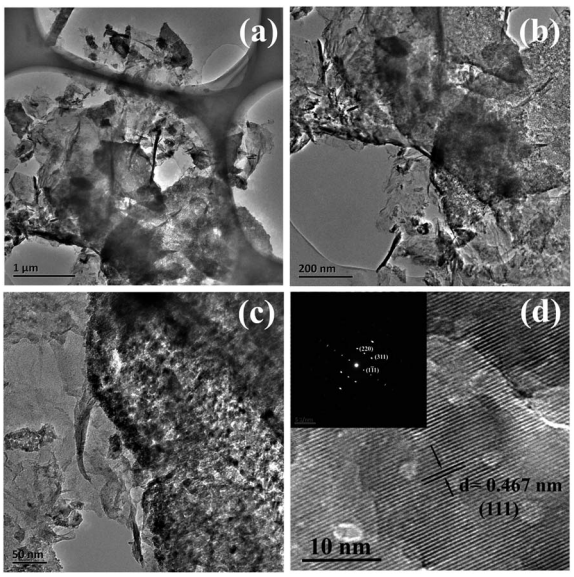

Fig. 6 (a–c) TEM images of the Co_3O_4/GS hybrid, (d) HRTEM image of Co_3O_4; the inset in (d) shows the corresponding SAED pattern.

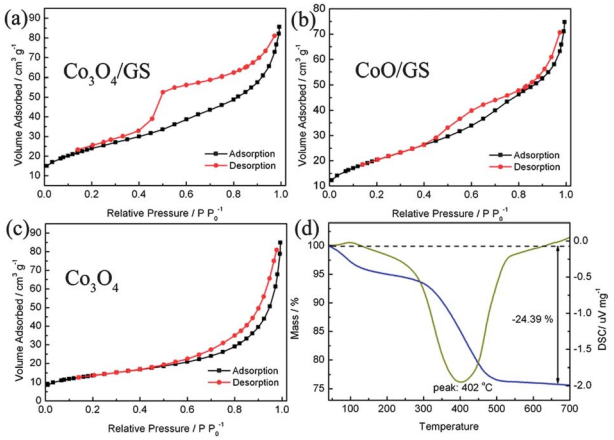

Fig. 7 (a–c) Nitrogen adsorption and desorption isotherms of Co_3O_4/GS, CoO/GS and pure Co_3O_4, respectively; (d) TG curve of Co_3O_4/GS hybrid films obtained from $Co(OH)_2$/GO films with a mass ratio of 1 : 1.

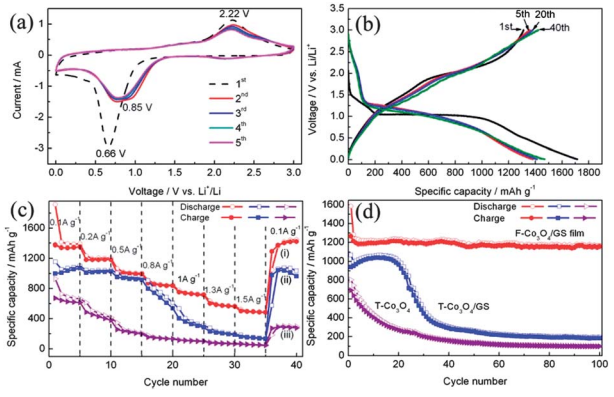

Fig. 8 (a) Cyclic voltammograms for the first five cycles of the F-Co_3O_4/GS electrode; (b) charge–discharge voltage profiles of the F-Co_3O_4/GS electrode at a current density of 100 mA g^{-1}; (c) the rate capability of F-Co_3O_4/GS (i), T-Co_3O_4/GS (ii) and T-Co_3O_4 (iii) at different current densities; (d) comparative cycle performance of electrodes at a current density of 200 mA g^{-1}.

Fig. 8b shows the representative charge–discharge profiles of Co_3O_4/GS at a current density of 100 mA g^{-1} between 0.01 and 3 V *vs.* Li^+/Li. In the first discharge curve, it showed a long voltage plateau at ~1.04 V followed by a sloping curve down to the cutoff voltage of 0.01 V, indicative of typical characteristics of voltage trends for the Co_3O_4 electrode.[10,25] The first discharge and charge capacities were as high as 1714 and 1312 mA h g^{-1} based on the total mass of composites (including graphene). The lithium storage capacities were much higher than the theoretical capacity of Co_3O_4 (890 mA h g^{-1}) owing to the formation of the SEI layer and possibly interfacial Li^+ storage.[45,53,68] A reversible capacity of 1379 mA h g^{-1} was achieved in the 5th cycle, which gradually increased to about 1422 mA h g^{-1} in the 40th cycle. Such an increase in capacity during cycling may be related to the gradual activation of the hybrid electrode, and was also observed in the previously reported results.[20,23,26]

To further demonstrate the superiority of the unique Co_3O_4/GS free-standing and binder-free electrode (denoted as F-Co_3O_4/GS) for lithium storage, traditional binder-enriched electrodes (with 10 wt% PVDF binder and 10 wt% carbon black) of pure Co_3O_4 and the hybrid of Co_3O_4/GS (denoted as T-Co_3O_4 and T-Co_3O_4/GS, respectively) were also fabricated by conventional slurry-coating technology. Fig. 8c displays the rate performance of the three electrodes. F-Co_3O_4/GS delivered very high capacity of 1390, 1203, 1005, 855, 735, 577 and 493 mA h g^{-1} at 100, 200, 500, 800, 1000, 1300 and 1500 mA g^{-1}, respectively. Remarkably, when the current density returned to 100 mA g^{-1}, a capacity of 1446 mA h g^{-1} was recovered. These values are higher than those previously reported.[16,36,38,39] However, the T-Co_3O_4 electrode showed much poorer rate capacity and cannot bear large current density due to the inefficient electron transport. T-Co_3O_4/GS reached a comparable capacity at low current density. Unfortunately, the charge storage capacity at high rates was not comparable to that of the free-standing and binder-less hybrid electrode. This may be due to two reasons. First, the presence of a polymer binder may block the diffusion channels of ion transportation.[14,28,41,42] Secondly, the grinding treatment of Co_3O_4/GS films into powders significantly destroyed the initial tight contact between Co_3O_4 and GS, and resulted in a weaker interfacial interaction. Therefore, constructing a binder-free, robust architecture of Co_3O_4/graphene is critical to achieve a high performance of the hybrid electrode.

Besides the high capacity and good rate capability, the F-Co_3O_4/GS electrode also showed excellent cycling stability (Fig. 8d). The charge–discharge capacities retained was ~1200 mA h g^{-1} at 200 mA g^{-1} without noticeable capacity loss during 100 cycles. The Coulombic efficiency of the first cycle was *ca.* 72% and from the second cycle onwards it remained above 98%, indicative of high charge–discharge reversibility of the anode material for LIBs (Fig. S4†). For T-Co_3O_4, the specific capacity decreased significantly and retained only ~100 mAh g^{-1} after 100 cycles. In the case of T-Co_3O_4/GS, though it showed much stable capacity during the initial 20 cycles, the stability degraded to only 250 mA h g^{-1} after 100 cycles. These results further imply that the graphene conductive network and free-standing electrode structure do result in better active material utilization and thus improved electrochemical properties.

In order to achieve an in-depth understanding of the advantages of binder-less and free-standing electrodes and the role of graphene, EIS was employed to investigate the electrochemical reaction kinetics of different electrodes (Fig. 9). The semicircle appeared in the medium frequency range is classically assigned to the charge-transfer resistance (R_{ct}) occurring between active materials and liquid electrolyte. The straight line is attributed to the diffusion of lithium ions into electrode materials, or the so-called Warburg diffusion[16,69] (Fig. 9a). For the T-Co_3O_4 electrode (Fig. 9b), R_{ct} was 19.34 Ω before cycling and increased dramatically to 34.22 Ω after ten cycles (ΔR_{ct} = 14.88 Ω), suggesting a considerable degradation of charge transfer kinetics. This may be due to the severe pulverization of Co_3O_4 and the loss of electric contact with the current collector. In the case of the T-Co_3O_4/GS electrode (Fig. 9c), R_{ct} was 15.56 Ω before cycling and increased less (ΔR_{ct} = 6.87 Ω) than the pure T-Co_3O_4 electrode. Evidently, the presence of graphene improved the conductivity of the electrode, effectively accommodated the volume change of Co_3O_4 and prevented its agglomeration during cycling. Therefore, the degradation of charge transfer kinetics was suppressed to some extent. By contrast, R_{ct} of the F-Co_3O_4/GS electrode was the smallest (13.31 Ω) before cycling (Fig. 9d), suggesting the lowest charge transfer resistance. And also, it decreased to 9.14 Ω after 10 cycles (ΔR_{ct} = −4.17 Ω), indicating good electrode stability with an activation process. This may be attributed to the unique architecture of the free-standing and binder-free Co_3O_4/GS electrode. On one hand, the charge transfer kinetics was improved since the use of electrically insulative polymer binder was avoided. On the other hand, the morphological compatibility coupled with strong interfacial interactions between Co_3O_4 and GS also significantly promoted the interfacial electron and lithium ion transport. Thirdly, unlike a traditional electrode, the free-standing electrode, which integrated active materials and the current collector (graphene) into one film, ensured durable electric contact of Co_3O_4 with the current collector. The above synergetic effect favors a large capacity, and good rate capability as well as superior cycle stability of F-Co_3O_4/GS.

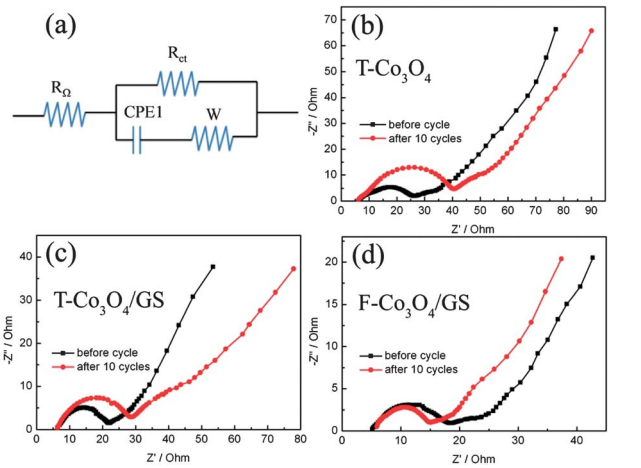

Fig. 9 (a) An equivalent circuit model of the electrodes, (b–d) Nyquist plots of T-Co_3O_4, T-Co_3O_4/GS and F-Co_3O_4/GS free-standing electrodes before and after ten cycles at a constant current density of 100 mA g^{-1}.

4 Conclusions

We have demonstrated an effective strategy to strengthen interfacial interactions by assembling 2D Co_3O_4 nanosheets with GS into a lamellar hierarchical structure with the assistance of electrostatic attractive interactions. As a binder-less and free-standing anode material, the Co_3O_4/GS hybrid achieved a high reversible capacity of ~1400 mA h g^{-1} at a current density of 100 mA g^{-1}. Moreover, the cycling performance and rate capability were significantly improved compared with a traditional electrode and a pure Co_3O_4 electrode. The superior electrochemical performance can be attributed to the following reasons. One is the short transport length for both lithium ions and electrons and the porous nature which favors electrolyte penetration. Another reason is the graphene 3D network, which prevents agglomeration of Co_3O_4 and enhances the structural stability and electrochemical reaction kinetics. More importantly, the morphological compatibility coupled with strong interfacial interactions between Co_3O_4 and GS significantly promoted the interfacial electron and lithium ion transport. This structural design approach offers an effective technique to boost electrochemical performances of electrode materials, and can be extended to synthesize other metal oxide/graphene hybrid anodes.

Acknowledgements

This work is supported by the 973 Project (2012CB932303), the National Natural Science Foundation of China (Grant no. 51172261).

Notes and references

1 B. Koo, H. Xiong, M. D. Slater, V. B. Prakapenka, M. Balasubramanian, P. Podsiadlo, C. S. Johnson, T. Rajh and E. V. Shevchenko, *Nano Lett.*, 2012, **12**, 2429–2435.
2 C. H. Xu, J. Sun and L. Gao, *J. Mater. Chem.*, 2012, **22**, 975–979.
3 A. M. Chockla, J. T. Harris, V. A. Akhavan, T. D. Bogart, V. C. Holmberg, C. Steinhagen, C. B. Mullins, K. J. Stevenson and B. A. Korgel, *J. Am. Chem. Soc.*, 2011, **133**, 20914–20921.
4 H. Kim, D.-H. Seo, H. Kim, I. Park, J. Hong, K.-Y. Park and K. Kang, *Chem. Mater.*, 2012, **24**, 720–725.
5 R. S. Ruoff, X. J. Zhu, Y. W. Zhu, S. Murali and M. D. Stollers, *ACS Nano*, 2011, **5**, 3333–3338.
6 R. Z. Li, X. Ren, F. Zhang, C. Du and J. P. Liu, *Chem. Commun.*, 2012, **48**, 5010–5012.
7 Q. H. Min, X. X. Zhang, H. Y. Zhang, F. Zhou and J. J. Zhu, *Chem. Commun.*, 2011, **47**, 11709–11711.
8 G. Jo, I. Choi, H. Ahn and M. Park, *Chem. Commun.*, 2012, **48**, 3987–3989.
9 X. L. Jia, Z. Chen, X. Cui, Y. T. Peng, X. L. Wang, G. Wang, F. Wei and Y. F. Lu, *ACS Nano*, 2012, **6**, 9911–9919.
10 N. Yan, L. Hu, Y. Li, Y. Wang, H. Zhong, X. Y. Hu, X. K. Kong and Q. W. Chen, *J. Phys. Chem. C*, 2012, **116**, 7227–7235.
11 X. C. Dong, H. Xu, X. W. Wang, Y. X. Huang, M. B. Chan-Park, H. Zhang, L. H. Wang, W. Huang and P. Chen, *ACS Nano*, 2012, **6**, 3206–3213.
12 H. B. Wu, J. S. Chen, H. H. Hny and X. W. Lou, *Nanoscale*, 2012, **4**, 2526–2542.
13 L. X. Lin and S. W. Zhang, *J. Mater. Chem.*, 2012, **22**, 14385–14393.
14 X. C. Chen, W. Wei, W. Lv, F. Y. Su, Y. B. He, B. H. Li, F. Y. Kang and Q. H. Yang, *Chem. Commun.*, 2012, **48**, 5904–5906.
15 X. Y. Feng, C. Shen, Y. Yu, S. Q. Wei and C. H. Chen, *J. Power Sources*, 2013, **230**, 59–65.
16 B. G. Choi, S.-J. Chang, Y. B. Lee, J. S. Bae, H. J. Kim and Y. S. Huh, *Nanoscale*, 2012, **4**, 5924–5930.
17 N. Du, H. Zhang, B. Chen, J. B. Wu, X. Y. Ma, Z. H. Liu, Y. Q. Zhang, D. Yang, X. H. Huang and J. P. Tu, *Adv. Mater.*, 2007, **19**, 4505–4509.
18 J. C. Huang, J. T. Zhu, K. Cheng, Y. Xu, D. X. Cao and G. L. Wang, *Electrochim. Acta*, 2012, **75**, 273–278.
19 C. C. Li, Q. H. Li, L. B. Chen and T. H. Wang, *J. Mater. Chem.*, 2011, **21**, 11867–11872.
20 W. M. Mei, J. Huang, L. P. Zhu, Z. Z. Ye, Y. J. Mai and J. P. Tu, *J. Mater. Chem.*, 2012, **22**, 9315–9323.
21 L. M. Wang, B. Liu, S. H. Ran, H. T. Huang, X. F. Wang, B. Liang, D. Chen and G. Z. Shen, *J. Mater. Chem.*, 2012, **22**, 23541–23546.
22 L. Hu, N. Yan, Q. W. Chen, P. Zhang, H. Zhong, X. R. Zheng, Y. Li and X. Y. Hu, *Chem.–Eur. J.*, 2012, **18**, 8971–8977.
23 X. H. Rui, H. T. Tan, D. H. Sim, W. L. Liu, C. Xu, H. H. Hng, R. Yazami, T. M. Lim and Q. Y. Yan, *J. Power Sources*, 2013, **222**, 97–102.
24 X. W. Lou, D. Deng, J. Y. Lee and L. A. Archer, *J. Mater. Chem.*, 2008, **18**, 4397–4401.
25 X. Wang, H. Guan, S. M. Chen, H. Q. Li, T. Y. Zhai, D. M. Tang, Y. Bando and D. Golberg, *Chem. Commun.*, 2011, **47**, 12280–12282.
26 F. M. Zhan, B. Y. Geng and Y. J. Guo, *Chem.–Eur. J.*, 2009, **15**, 6169–6174.
27 C. Z. Yuan, L. Yang, L. R. Hou, L. F. Shen, X. G. Zhang and X. W. Lou, *Energy Environ. Sci.*, 2012, **5**, 7883–7887.
28 L. Noerochim, J. Z. Wang, S. L. Chou, D. Wexler and H. K. Liu, *Carbon*, 2012, **50**, 1289–1297.
29 S. L. Xiong, J. S. Chen, X. W. Lou and H. C. Zeng, *Adv. Funct. Mater.*, 2011, **22**, 861–871.
30 P. Zhang, Z. P. Guo, Y. D. Huang, D. Z. Jia and H. K. Liu, *J. Power Sources*, 2011, **196**, 6987–6991.
31 X. Zhao, C. M. Hayner, M. C. Kung and H. H. Kung, *ACS Nano*, 2011, **5**, 8739–8749.
32 W. F. Chen, S. R. Li, C. H. Chen and L. F. Yan, *Adv. Mater.*, 2011, **23**, 5679–5683.
33 H. L. Wang, Y. Yang, Y. Y. Liang, L. F. Cui, H. S. Casalongue, Y. G. Li, G. S. Hong, Y. Cui and H. J. Dai, *Angew. Chem., Int. Ed.*, 2011, **50**, 7364–7368.
34 R. H. Wang, Y. Wang, C. H. Xu, J. Sun and L. Gao, *RSC Adv.*, 2013, **3**, 1194–1200.
35 L. Q. Tao, J. T. Zai, K. X. Wang, H. J. Zhang, M. Xu, J. Shen, Y. Z. Su and X. F. Qian, *J. Power Sources*, 2012, **202**, 230–235.

36 B. J. Li, H. Q. Cao, J. Shao, G. Q. Li, M. Z. Qu and G. Yin, *Inorg. Chem.*, 2011, **50**, 1628–1632.
37 G.-P. Kim, I. Nam, N. D. Kim, J. Park, S. Park and J. Yi, *Electrochem. Commun.*, 2012, **22**, 93–96.
38 H. Kim, D.-H. Seo, S.-W. Kim, J. Kim and K. Kang, *Carbon*, 2011, **49**, 326–332.
39 Z. S. Wu, W. C. Ren, L. Wen, L. B. Gao, J. P. Zhao, Z. P. Chen, G. M. Zhou, F. Li and H. M. Cheng, *ACS Nano*, 2010, **4**, 3187–3194.
40 X. L. Yang, K. C. Fan, Y. H. Zhu, J. H. Shen, X. Jiang, P. Zhao and C. Z. Li, *J. Mater. Chem.*, 2012, **22**, 17278–17283.
41 H. Gwon, H. S. Kim, K. U. Lee, D. H. Seo, Y. C. Park, Y. S. Lee, B. T. Ahn and K. Kang, *Energy Environ. Sci.*, 2011, **4**, 1277–1283.
42 Z. P. Li, Y. J. Mi, X. H. Liu, S. Liu, S. R. Yang and J. Q. Wang, *J. Mater. Chem.*, 2011, **21**, 14706–14711.
43 F. Xiao, Y. Q. Li, X. L. Zan, K. Liao, R. Xu and H. W. Duan, *Adv. Funct. Mater.*, 2012, **22**, 2487–2494.
44 C. Z. Yuan, L. Yang, L. R. Hou, J. Y. Li, Y. X. Sun, X. G. Zhang, L. F. Shen, X. J. Lu, S. L. Xiong and X. W. Lou, *Adv. Funct. Mater.*, 2012, **22**, 2560–2566.
45 T. Hu, X. Sun, H. T. Sun, M. P. Yu, F. Y. Lu, C. S. Liu and J. Lian, *Carbon*, 2013, **51**, 322–326.
46 A. P. Yu, H. W. Park, A. Davies, D. C. Higgins, Z. W. Chen and X. C. Xiao, *J. Phys. Chem. Lett.*, 2011, **2**, 1855–1860.
47 J. W. Lee, S. Y. Lim, H. M. Jung, T. H. Hwang, J. K. Kang and J. W. Choi, *Energy Environ. Sci.*, 2012, **5**, 9889–9894.
48 X. Zhao, C. M. Hayner, M. C. Kung and H. H. Kung, *Adv. Energy Mater.*, 2011, **1**, 1079–1084.
49 B. Wang, X. L. Li, B. Luo, Y. Y. Jia and L. J. Zhi, *Nanoscale*, 2013, **5**, 1470–1474.
50 B. Wang, X. L. Li, X. F. Zhang, B. Luo, M. H. Jin, M. H. Liang, S. A. Dayeh, S. T. Picraux and L. J. Zhi, *ACS Nano*, 2013, **7**, 1437–1445.
51 S. M. Paek, E. Yoo and I. Honma, *Nano Lett.*, 2009, **9**, 72–75.
52 J. Z. Wang, C. Zhong, S. L. Chou and H. K. Liu, *Electrochem. Commun.*, 2010, **12**, 1467–1470.
53 R. H. Wang, C. H. Xu, J. Sun, L. Gao and C. C. Lin, *J. Mater. Chem. A*, 2013, **1**, 1794–1800.
54 Z. P. Liu, R. Z. Ma, M. Osada, K. Takada and T. Sasaki, *J. Am. Chem. Soc.*, 2005, **127**, 13869–13874.
55 W. S. Hummers and R. E. Offeman, *J. Am. Chem. Soc.*, 1958, **80**, 1339.
56 X. S. Zhou, Y. X. Yin, L. J. Wan and Y. G. Guo, *Adv. Energy Mater.*, 2012, **2**, 1086–1090.
57 J. S. Lee, K. H. You and C. B. Park, *Adv. Mater.*, 2012, **24**, 1084–1088.
58 J. S. Chen, Z. Wang, X. C. Dong, P. Chen and X. W. Lou, *Nanoscale*, 2011, **3**, 2158–2161.
59 W. W. Zhou, J. X. Zhu, C. W. Cheng, J. P. Liu, H. P. Yang, C. X. Cong, C. Guan, X. T. Jia, H. J. Fan, Q. Y. Yan, C. M. Li and T. Yu, *Energy Environ. Sci.*, 2011, **4**, 4954–4961.
60 J. Y. Zhu and J. H. He, *ACS Appl. Mater. Interfaces*, 2012, **4**, 1770–1776.
61 C. Z. Zhu, Y. X. Fang, D. Wen and S. J. Dong, *J. Mater. Chem.*, 2011, **21**, 16911–16917.
62 J. K. Chang, C. M. Wu and I. W. Sun, *J. Mater. Chem.*, 2010, **20**, 3729–3735.
63 N. N. Binitha, P. V. Suraja, Z. Yaakob, M. R. Resmi and P. P. Silija, *J. Sol-Gel Sci. Technol.*, 2010, **53**, 466–469.
64 G. Q. Zhang and X. W. Lou, *Sci. Rep.*, 2013, **3**, 1470.
65 G. Q. Zhang and X. W. Lou, *Adv. Mater.*, 2013, **25**, 976–979.
66 Y. J. Fu, X. W. Li, X. L. Sun, X. H. Wang, D. Q. Liu and D. Y. He, *J. Mater. Chem.*, 2012, **22**, 17429–17431.
67 J. Chen, X. H. Xia, J. P. Tu, Q. Q. Xiong, Y. X. Yu, X. L. Wang and C. D. Gu, *J. Mater. Chem.*, 2012, **22**, 15056–15061.
68 L. H. Zhuo, Y. Q. Wu, J. Ming, L. Y. Wang, Y. C. Yu, X. B. Zhang and F. Y. Zhao, *J. Mater. Chem. A*, 2013, **1**, 1141–1147.
69 C. T. Hsieh, J. S. Lin, Y. F. Chen and H. Teng, *J. Phys. Chem. C*, 2012, **116**, 15251–15258.